

Rotor Eddy Current Loss Reduction with Permeable Retaining Sleeve for Permanent Magnet Synchronous Machine

Zhu, Zichong; Huang, Yunkai; Dong, Jianning; Peng, Fei; Yao, Yu

DOI

[10.1109/TEC.2020.2966674](https://doi.org/10.1109/TEC.2020.2966674)

Publication date

2020

Document Version

Final published version

Published in

IEEE Transactions on Energy Conversion

Citation (APA)

Zhu, Z., Huang, Y., Dong, J., Peng, F., & Yao, Y. (2020). Rotor Eddy Current Loss Reduction with Permeable Retaining Sleeve for Permanent Magnet Synchronous Machine. *IEEE Transactions on Energy Conversion*, 35(2), 1088-1097. Article 8959123. <https://doi.org/10.1109/TEC.2020.2966674>

Important note

To cite this publication, please use the final published version (if applicable). Please check the document version above.

Copyright

Other than for strictly personal use, it is not permitted to download, forward or distribute the text or part of it, without the consent of the author(s) and/or copyright holder(s), unless the work is under an open content license such as Creative Commons.

Takedown policy

Please contact us and provide details if you believe this document breaches copyrights. We will remove access to the work immediately and investigate your claim.

Green Open Access added to TU Delft Institutional Repository

'You share, we take care!' - Taverne project

<https://www.openaccess.nl/en/you-share-we-take-care>

Otherwise as indicated in the copyright section: the publisher is the copyright holder of this work and the author uses the Dutch legislation to make this work public.

Rotor Eddy Current Loss Reduction With Permeable Retaining Sleeve for Permanent Magnet Synchronous Machine

Zichong Zhu ¹, Student Member, IEEE, Yunkai Huang ¹, Jianning Dong ¹, Member, IEEE, Fei Peng, Member, IEEE, and Yu Yao ¹, Student Member, IEEE

Abstract—This article presents a new rotor design to reduce rotor eddy current loss of a high-speed permanent magnet synchronous machine for flywheel energy storage system. Instead of using common nonmagnetic sleeves, the new rotor incorporates permeable retaining sleeves (PRSs) to fix permanent magnets on the rotor hub. The PRSs are made of permalloy that features high permeability and high electrical conductivity. Thus, skin depths for asynchronous harmonics are extremely small. On the other hand, the PRSs are electrically insulated along the circumferential direction. Owing to these two reasons, rotor eddy current loss at open circuit decreases by 64.2% without sacrificing torque output, compared with an original rotor with nonmagnetic retaining sleeve. In addition, thermal and structural finite element analyses are performed to calculate rotor temperature distribution and evaluate the structural integrity of the new rotor. Rotor eddy current loss reduction benefits lowering rotor temperature rise. Prototype machine with the new rotor is fabricated, and preliminary tests are carried out to confirm the analysis results.

Index Terms—Eddy current, high-speed machine, permeable retaining sleeve (PRS), permanent-magnet machine, rotor loss reduction.

I. INTRODUCTION

HIGH-SPEED permanent magnet synchronous machines (HSPMSMs) receive more attention lately in applications such as air compression, micro-machining, and flywheel energy storage system [1], [2]. This kind of machine features high power density, excellent dynamic performance, and high efficiency. Due to the low tensile strength of silicon steel sheet and severe flux leakage at rotor bridges, interior permanent magnet rotor is considered inappropriate for HSPMSM [3]. Surface-mounted permanent magnet machine (SPM) is usually used accounting for its excellent rotor integrity and rigidity.

Common rotor topologies for SPM are shown in Fig. 1. To counteract the centrifugal force of permanent magnets (PMs)

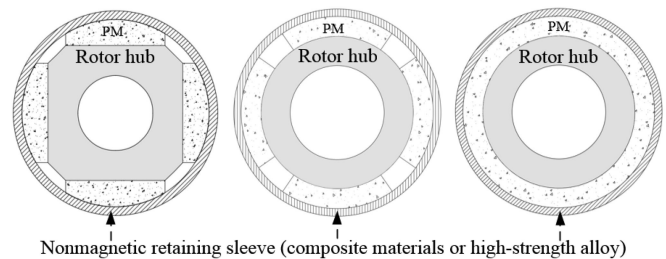


Fig. 1. Commonly used rotor structures in HSPMSMs.

during high-speed operation, a thick nonmagnetic retaining sleeve (NRS) is usually necessary. The presence of NRS lengthens the effective air gap and increases the reluctance of the main magnetic circuit. Consequently, the air-gap flux density is lowered, and large eddy current loss is produced in NRS when it is made of metallic material.

Commonly used materials for NRS include carbon fiber composite [4], glass fiber composite [5], and high-strength alloys, such as Inconel 718 [6] and titanium alloy [7]. Using a composite sleeve can reduce eddy current loss in the sleeve itself, but inevitably increases this loss in PMs [8]. Meanwhile, the small thermal conductivity of composite materials hinders heat dissipation from PMs to the air gap, which may cause a large temperature rise and thus poor magnetic properties of PM [9]. In addition, the material and tooling costs of composite sleeves are expected to be high.

Methods used to suppress rotor eddy current and reduce associated loss include slotless stator [10], axial segmentation of NRS or PMs [11], winding configuration optimization [11], multilayer retaining sleeve [9], and copper cladding [12]. These solutions usually sacrifice torque output or increase PM usage.

New structures and materials for retaining sleeve are also proposed. By grooving retaining sleeve in the circumferential direction, rotor eddy current loss decreases by 23% [7]. Whereas such grooves may deteriorate rotor strength and bring rotor dynamic problem. A novel retaining sleeve is presented in [6], which looks like a skewed cast aluminum rotor cage of the induction machine. The eddy current flow path veers and associated loss is effectively reduced. Nevertheless, this structure may cause more eddy current loss in PMs and the strength of it is not fully evaluated.

Manuscript received September 16, 2019; revised December 18, 2019; accepted January 8, 2020. Date of publication January 14, 2020; date of current version May 20, 2020. This work was supported by the National Natural Science Foundation of China under Grant 51777034. Paper no. TEC-00938-2019. (Corresponding author: Yunkai Huang.)

Z. Zhu, Y. Huang, F. Peng, and Y. Yao are with the School of Electrical Engineering, Southeast University, Nanjing 210096, China (e-mail: zichong_zhu@seu.edu.cn; huangyk@seu.edu.cn; pengfei@seu.edu.cn; yuyao@seu.edu.cn).

J. Dong is with the Faculty of Electrical Engineering, Mathematics & Computer Science, Delft University of Technology, 2628CD Delft, Netherlands (e-mail: j.dong-4@tudelft.nl).

Color versions of one or more of the figures in this article are available online at <https://ieeexplore.ieee.org>.

Digital Object Identifier 10.1109/TEC.2020.2966674

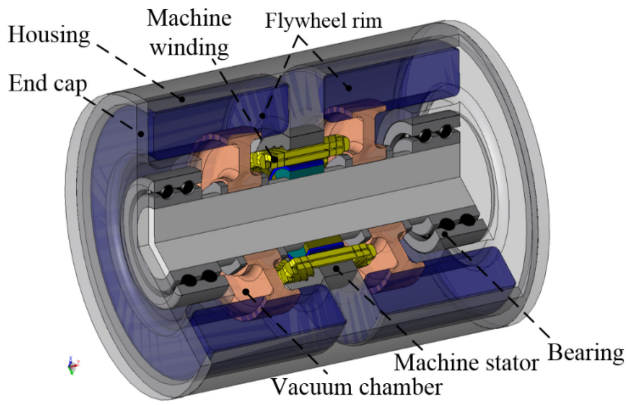


Fig. 2. Structure of the 2.5 kW, 0.5 kWh FESS with surface-mounted permanent magnet HSPMSM.

To increase the open-circuit air-gap flux density, a retaining sleeve made of semi-permeable material is used in [13]. It shows that the fundamental component of the electromotive force (EMF) increases more than 20%, compared with that using magnetically inert retaining sleeve. To reduce eddy current loss, the retaining sleeve is made by 2 mm thick axially-laminated cold-worked steel sheet (relative permeability $\mu_r = 6$). Comparative study on machines with retaining sleeve made of Fe-20%Cu alloy (maximal relative permeability $\mu_{rmax} = 59$) and nonmagnetic materials mentioned above is presented in [14]. It found that using the Fe-20%Cu alloy even decreases air-gap flux density, because considerable PM flux is “short-circuited” by the semi-permeable material. Also, this kind of material has low electrical resistivity, which induces more rotor eddy current loss.

This paper presents a new rotor design with permeable retaining sleeve (PRS) for an HSPMSM developed for flywheel energy storage system (FESS). Proposed rotor topology aims at reducing rotor eddy current loss, without sacrificing torque output. This loss is difficult to be dissipated outside since the rotor is installed in a high-vacuum chamber. Moreover, rotor loss reduction is vital for lowering the idling loss and increasing the round-trip efficiency of FESS. Electromagnetic performance of machines with the original and proposed rotors are comparatively studied, as given in section II-IV. 3-D finite element analysis (FEA) is used due to the complicated geometry and stray flux of the new rotor. Section V presents the rotor temperature distribution calculated by thermal FEA to keep PM temperature under permitted value. Structural FEA is carried out to evaluate the mechanical integrity of the new rotor in section VI, where thermal stress is considered by directly importing rotor temperature distribution from the thermal analysis. A prototype is fabricated, and preliminary tests are performed to confirm the analysis results and magnetic circuit characterization.

II. ORIGINAL AND PROPOSED ROTORS

A. Original Machine

The investigated 0.5 kWh, 2.5 kW FESS is shown in Fig. 2. The motor/generator is installed inside the composite rim with limited axial space, and thus the total length of end windings and

TABLE I
DESIGN SPECIFICATIONS OF THE INVESTIGATED FESS

Rated power (kW)	2.5	Maximum speed (r/min)	22500
Rated current (A)	18	Envelope dimension (mm)	$\Phi 130 \times 80$
Ambient temperature ($^{\circ}\text{C}$)	≤ 40	Depth of discharge (%)	75
Idling loss (W)	≤ 80	Idling rotor loss (W)	≤ 25

TABLE II
DESIGN PARAMETERS OF THE HSPMSM

Number of poles	4	Number of slots	24
Rated power (kW)	2.5	Maximum speed (r/min)	22500
PM thickness (mm)	7	Winding layers	2
Turns per coil	5	Parallel paths per phase winding	2
Diameter of stator (mm)	130	Diameter of stator bore (mm)	80
Stator stack length (mm)	30	Physical air gap (mm)	1.5

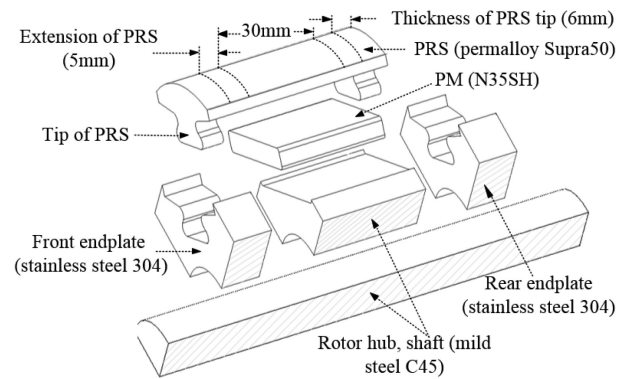


Fig. 3. Proposed rotor structure (quadrant) and materials of each part.

the stator lamination is of upper limit. Design specifications of the FESS are listed in Table I. The original HSPMSM developed for this FESS uses common rotor topology, as in Fig. 1 (middle). Surface-mounted PMs are fixed on the solid rotor hub by a non-magnetic metallic retaining sleeve via interference fit. Though with small rotor diameter, to counteract huge centrifugal force at high-speed rotation, a 2.5 mm thick retaining sleeve made of stainless steel 304 is used. Design parameters are given in Table II. To reduce rotor eddy current loss, a large air gap of 1.5 mm is used. However, this kind of loss is still too much to meet idling rotor loss requirement.

B. Proposed Machine

A new rotor structure is proposed to suppress rotor eddy current and reduce associated loss, as shown in Fig. 3. Integral NRS in the original rotor is replaced with 4 PRSs. The PRS made of permalloy is connected to nonmagnetic end plates via keyways, which are made of stainless steel 304. To eliminate local stress concentration, rectangular instead of arc-shaped magnets are used. The axial air gap between the rotor end and the tip of PRS (the extension of PRS) is 5 mm, designed to reduce rotor end flux leakage. Grooves are machined on the rotor hub to install PMs and protect them from translation during acceleration or deceleration.

Cross-sections of the original and proposed rotors are shown in Fig. 4. Arc-shaped PMs that are parallelly magnetized are

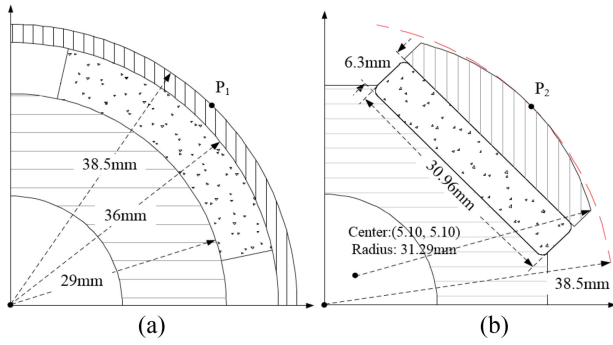


Fig. 4. Cross-sections of the original and proposed rotors (quadrant). (a) Original rotor. (b) Proposed rotor.

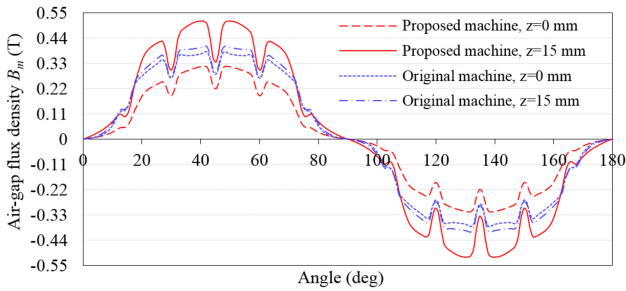


Fig. 5. Open-circuit air-gap flux densities in both machines from 3-D FEA (20 °C).

employed in the original rotor to excite more sinusoidal open-circuit air-gap flux density and back EMF. In the new rotor, the open-circuit air-gap flux density is optimized by parametric sensitivity analysis using 3-D finite element method. By reshaping the cylindrical surface of the PRS, an unequal air gap is formed. As shown in Fig. 4(b), the center of the cylindrical surface facing air gap misaligns with the rotor pivot point. Meanwhile, it has a radius smaller than that of the rotor.

Electromagnetic performances including back EMF, torque output, phase inductance and rotor eddy current loss are comparatively researched for these two rotors in next sections. For fair comparisons, the stator core, winding parameters, and physical air gap are kept unchanged.

III. BACK EMF AND INDUCTANCE COMPARISON

A. Back EMF

Since the NRS between the stator core and PMs in the original machine is replaced by permeable parts, the effective air gap is downsized. As a result, the reluctance of the main magnetic circuit is reduced, and PM usage is therefore reduced when exciting similar air-gap flux densities. As shown in Fig. 4(b), PM thickness decreases from 7 mm to 6.3 mm when producing the same back EMF as the original machine, while PM usage reduces by 25% from 0.24 kg to 0.18 kg, which helps to reduce the material cost of the FESS.

Fig. 5 plots the radial component of open-circuit air-gap flux density B_m at $z = 0$ mm and $z = 15$ mm (define the axial symmetry plane as the xy -plane of 3-D Cartesian coordinate

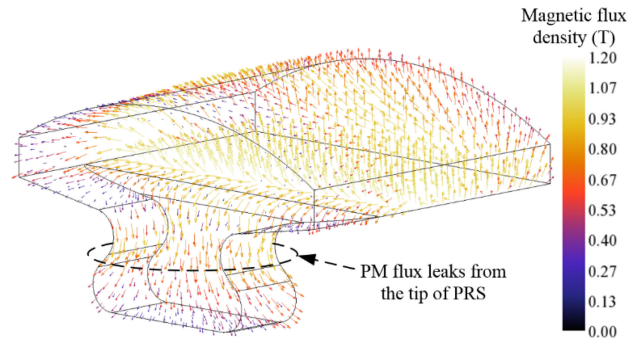


Fig. 6. PM flux leaks from the tip of PRS at open circuit.

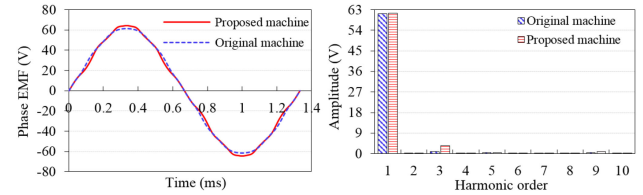


Fig. 7. Open-circuit phase EMFs and their spectra at 22500 r/min, 20 °C.

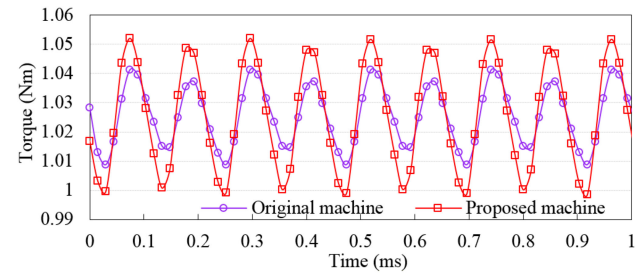


Fig. 8. Torque waveforms of the original and new machines with 25 A phase current.

system). It can be seen that B_m at $z = 0$ mm and $z = 15$ mm show obvious difference in the new machine, which doesn't appear in the original machine. B_m at the rotor end is larger than that of the original machine, but smaller on the symmetry plane. This means that B_m varies significantly along the axial direction due to the fact that more PM flux tends to leak from the rotor ends after introducing PRSs.

Fig. 6 illustrates the PM flux leaks from the tip of the PRS. The total flux provided by a half PM pole is 0.45 mWb. Flux leakage at a tip of PRS is 0.08 mWb, i.e., nearly 18.0% of PM flux doesn't link with the stator windings and excite back EMF. Fortunately, since the PRS reduces the effective air gap, PMs in the new rotor produce more flux than the original rotor. To be exact, rotor flux produced by a half PM pole in the original and new machines are 0.38 mWb and 0.45 mWb respectively. Thus, though with more flux leakage at the rotor ends, the PM flux links with the stator windings in the new rotor is still close to that of the original machine. Consequently, these two machines have similar back EMFs and torque constants.

Fig. 7 shows the phase EMFs and their spectra of the original and new machines. Fig. 8 presents the electromagnetic torque waveforms. As mentioned above, PM thickness and width in

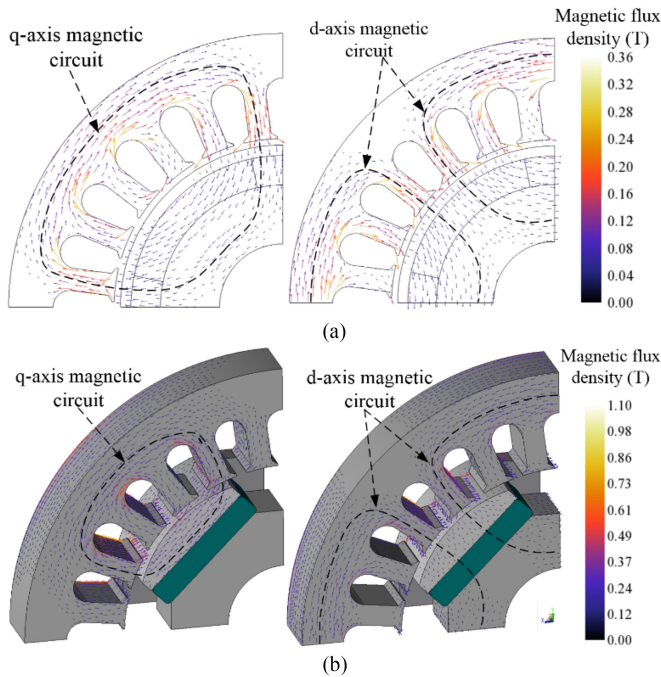


Fig. 9. Magnetic flux distributions when feeding only d- or q-axis current. (a) Original machine. (b) Proposed machine.

the new rotor are revised to keep back EMF and torque output unchanged. It can be seen from Fig. 7, the 3rd and 9th harmonics of the new machine are nearly triply increased. Fortunately, these harmonics will not appear in line voltage with star-connected windings. Compared with the original one, the new machine has almost same average torque, but a larger torque ripple due to the reduced air gap.

B. Inductance Increment

Along with reducing the main magnetic circuit reluctance, using PRS changes the flow paths of d- and q-axis flux. Fig. 9 shows the vector plot of flux induced by d- or q-axis current of 25 A. In the original machine, q-axis flux goes through the stator core, air gap, NRS, PM, and rotor hub successively, and then goes back to close the flow path. Whereas in the new rotor, q-axis flux traverses the PRS, yet bypasses the PM and rotor hub.

For the d-axis magnetic circuit, the original machine has similar d-axis flux flow path to that of the q-axis flux. However, things are different in the new rotor. Unlike the q-axis flux, the majority of d-axis flux still goes through PM, as shown in Fig. 9(b). Thus, in the new rotor, the d- and q-axis fluxes have different flow paths and reluctances.

As a result, d-axis inductance L_d and q-axis inductance L_q are both increased, due to the smaller magnetic circuit reluctances. More specially, with the same winding configuration, L_d increases from 45.4 μH to 67.1 μH , while L_q nearly doubles from 47.4 μH to 85.3 μH . The inductance increment may help to reduce current harmonics caused by the relatively small inductance of HSPMSM and limited switching frequency of power semi-conductors.

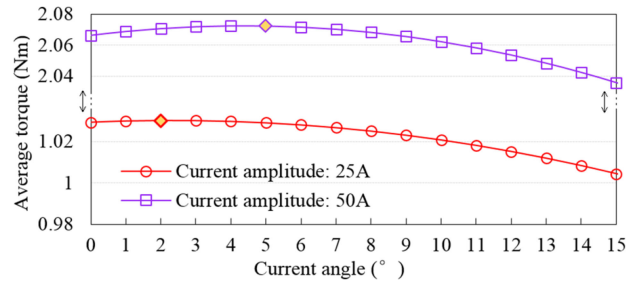


Fig. 10. The variation of average torque against current angles (angles advancing the back EMF).

It is noteworthy that the new rotor shows salient behavior since L_d and L_q are different. In theory, reluctance torque can be used to enhance the torque output by the maximum torque per ampere control. The variation of average torque against current angles is calculated by 3-D FEA and presented in Fig. 10. It can be seen that, the current angle where maximum torque appears is about 2° when feeding a 25 A phase current into the stator windings. Meanwhile, the average torque increases only 0.08% from 1.0294 Nm to 1.0302 Nm when current angle increases from 0° to 2°. In other words, the reluctance torque contribute little to torque output of the new machine. The reason is that, in the HSPMSM with surface-mounted permanent magnet rotor, the phase inductance is quite small. As a result, the PM flux linkage ψ_m is dominant, compared with the one excited by armature windings. Though the inductance increment of the new rotor is significant, the second right-hand term of (1) is still far smaller than the first one.

Certainly, a larger current helps to increase the portion of reluctance torque, but the increment is not obvious. For example, when the phase current increases to 50 A, the reluctance torque is only 0.4% of the total torque at current angle of 5°, as in Fig. 10. Thus, the maximum torque per ampere control is not used in the new machine.

$$T = \frac{3p}{2} [\psi_m i_q + (L_d - L_q) i_d i_q] \quad (1)$$

In addition, the inductance increment inevitably lowers the power factor and increases the voltage regulation ratio in generating mode. However, in HSPMSM with surface-mounted permanent magnet rotor, the inductance is small. Voltage drop on phase inductance is subordinate to the back EMF. For example, at the rated point, the amplitude of the phase EMF is 64.95 V. while, the voltage drop on phase inductance increases from 5.58 V to 10.05 V, due to the inductance increment. Consequently, the power factor decreases from 0.996 to 0.988. In the generating mode, the terminal voltage regulation ratio increases from 0.38% to 1.2% due to the inductance increment. Conclusively, the inductance increment of the new machine has minor influence on power factor and voltage regulation ratio.

IV. ROTOR EDDY CURRENT LOSS REDUCTION

Permeance harmonics, the spatial harmonics of magnetomotive force (MMF) and harmonics due to non-sinusoidal current induce the eddy current in conductive rotor parts, and thus

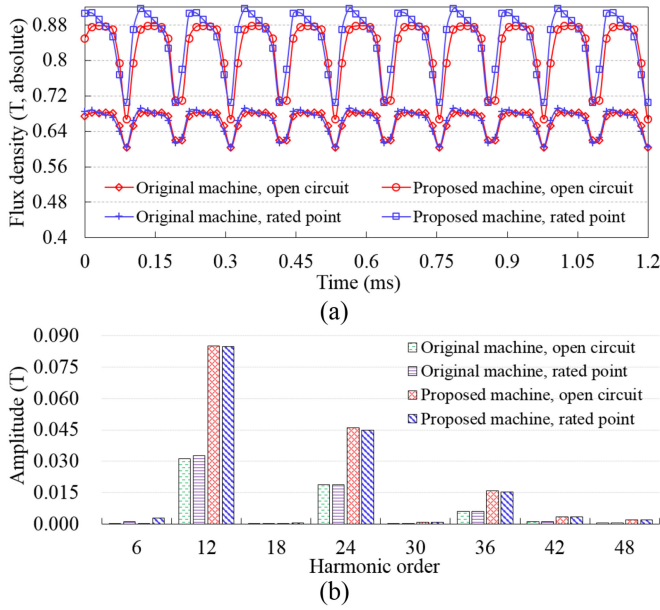


Fig. 11. Flux density variations on the surface of the NRS and PRS from 2-D FEA. (a) Flux density variations. (b) Spectra.

produce ohmic loss [15], [16]. To reduce current waveform distortion, high switching frequency SiC inverter equipped with output filters is developed for this application. Therefore, the third source is subordinate and can be neglected.

Fig. 11 shows flux density variations on the surface of retaining sleeves (P_1 and P_2 in Fig. 4) from 2-D FEA and their spectra, when assuming the retaining sleeves non-conductive. It can be seen from Fig. 11(b), the 12th and 24th harmonics are dominant, and both of them are significantly increased due to a smaller effective air gap after introducing the PRS.

The PRS is made of permalloy that features higher permeability μ_r and electrical conductivity σ , compared with the NRS made of 304 steel. As a result, the PRS produces extremely small skin depth δ for rotor asynchronous harmonics, as in (2), and damps these harmonics by induced eddy current while the synchronous field is not affected.

$$\delta = \sqrt{\frac{1}{\pi f \sigma \mu_r \mu_0}} \quad (2)$$

Due to a smaller δ , eddy current is confined to the surface of the PRS, which helps to reduce associated ohmic loss. This phenomenon is referred to as the shielding effect. In [12], [14], and [17], the shielding effect is realized by a copper cladding that has high electrical conductivity. Similarly, it can also be acquired with high-permeability materials, such as permalloy investigated in this paper.

Table III lists the electrical conductivity and relative permeability of permalloy, copper, and 304 steel, which are sourced from the product manuals of the manufacturers. Though the electrical conductivity of copper is nearly 27 times higher than that of permalloy, its relative permeability is only 1/54000 of that of its competitor. This indicates retaining sleeve made of permalloy has better shielding ability than a copper cladding.

TABLE III
RELATIVE PERMEABILITY AND ELECTRICAL CONDUCTIVITY OF
RETAINING SLEEVE MATERIALS

	Electrical conductivity σ (S/m)	Relative impedance permeability μ_r
Permalloy (Supra 50)	2.22e6	54000 (0.8T)
Copper	5.99e7	1
Stainless steel 304	1.39e6	1

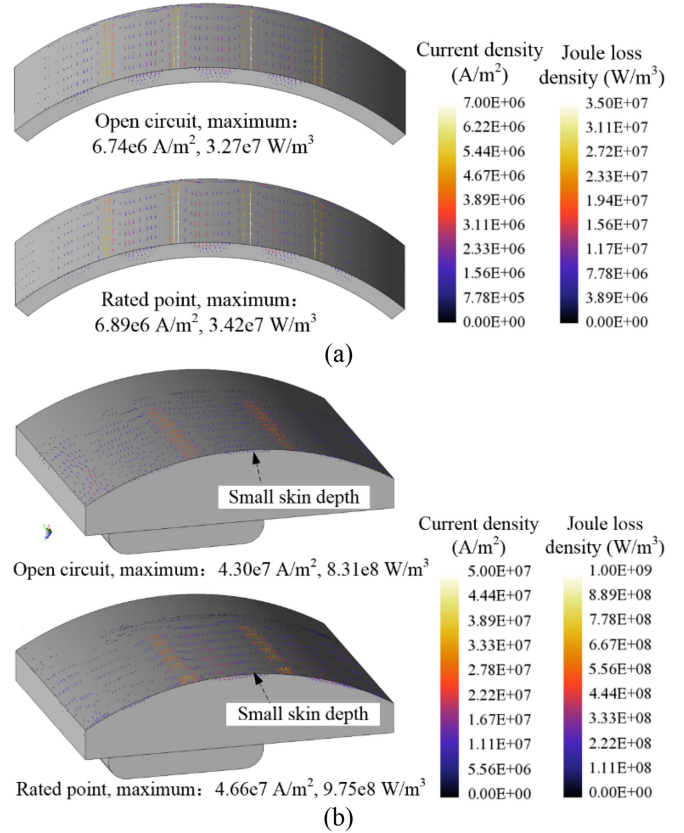


Fig. 12. Eddy current and related loss distributions. (a) NRS of the original rotor. (b) PRS of the new rotor.

For example, the skin depth of the 6th harmonic for permalloy, copper and 304 steel are 0.022 mm, 0.97 mm and 6.36 mm respectively.

To calculate the induced rotor eddy current accurately, 3-D FEA is used, because the magnetic field in rotor with short axial length shows more 3-D behavior, particularly in the new rotor, as shown in Fig. 6. Rotor eddy current and related loss distributions at open circuit and rated point in the NRS and PRS are shown in Fig. 12. The open-circuit results are calculated with no power supply, and the rated point has phase current of 25A and rotation speed of 22500 r/min.

The maximum eddy current density at open circuit increases from 6.74e6 A/m² to 4.30e7 A/m² after introducing the PRS. The same trend is observed for related loss density, which increases from 3.27e7 W/m³ to 8.31e8 W/m³. However, owing to a smaller skin depth, the region of high eddy current density is dramatically narrowed down. In addition, permalloy has a larger electrical conductivity than 304 steel, which also helps

TABLE IV
EDDY CURRENT LOSS IN EACH ROTOR PART (O₁: ORIGINAL ROTOR AT OPEN CIRCUIT, R₁: ORIGINAL ROTOR AT RATED POINT, O₂: PROPOSED ROTOR AT OPEN CIRCUIT, AND SO ON)

Eddy current loss	O ₁	R ₁	O ₂	R ₂
Retaining sleeve (W)	17.35	18.86	6.21	8.35
PMs (W)	0.18	0.20	0.02	0.03
Rotor hub (W)	0.02	0.02	0	0
Inter-pole wedges (W)	0.01	0.12	-	-
End plates (W)	-	-	0.06	0.14
Total loss (W)	17.56	19.24	6.29	8.52

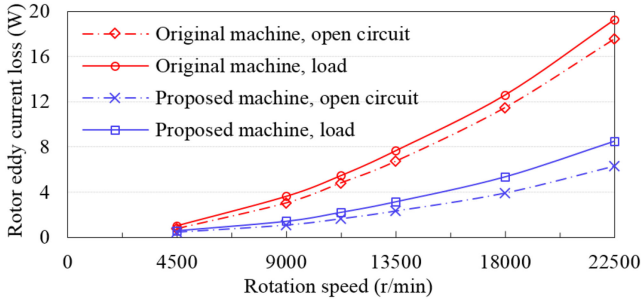


Fig. 13. Total rotor eddy current loss at different rotation speed from 3-D FEA.

to reduce eddy current loss P_{re} , as in (3), where J_e is the eddy current density.

$$P_{re} = \frac{1}{\sigma} \int_V J_e^2 dV \quad (3)$$

Table IV lists calculated eddy current loss in each rotor part at open circuit and rated point. It can be seen that, in both rotors, the majority of eddy current loss appears in conductive retaining sleeves. Most importantly, the eddy current loss in the new rotor decreases significantly. At open circuit, it reduces by 64.2% from 17.56 W to 6.29 W. Under load condition, it decreases from 19.24 W to 8.52 W. In addition, it deserves to be noted that, in both rotors, on-load eddy current loss increases not obviously compared with that at open circuit. It can be inferred that the spatial harmonics of MMF have less effect than permeance harmonics on rotor eddy current and associated loss.

Fig. 13 presents the variation of total rotor eddy current loss at different rotation speed. It can be seen that, in both machines, this kind of loss increases sharply with rotation speed at open circuit and on-load operation. Moreover, eddy current loss reduction in the new rotor appears at all speeds.

V. ROTOR TEMPERATURE RISE

3-D thermal FEA is carried out to confirm that the PM temperature is under the permitted value. The duty cycle of the FESS determines the round-trip loss and rotor temperature rise. This FESS has short on-load stages (charging or discharging). In addition, the solid rotor has a large heat capacity. Therefore, transient temperature rise during charging and discharging stages is not large. Nevertheless, for conservative estimation, on-load rotor loss density, instead of open-circuit one, is referenced as the

TABLE V
MECHANICAL AND THERMAL PROPERTIES OF EACH ROTOR PARTS

	Endplate	PRS	PM	Rotor hub +shaft
Density (g/cm ³)	7.85	8.2	7.5	7.8
Thermal conductivity (W/(m·K))	14.8	13.0	7.6	46.6
Specific heat (J/(kg·K))	485	500	460	467
Young's modulus (GPa)	192	140	155	202.2
Poisson's ratio	0.33	0.30	0.27	0.30
Thermal expansion coefficient (10 ⁻⁶ /K)	8.2	8.0	5.2	11.6

distributed heat source for thermal FEA in the two-way coupled analysis.

The motor/generator of the FESS is installed inside the chamber of high vacuum to reduce windage loss. However, heat dissipation from rotor surfaces to stator parts by air convection is unavailable under high vacuum condition. Moreover, due to the small temperature differences between various assemblies of the FESS, the analysis neglects radiative heat transfer in the chamber, and assumes all rotor losses are transferred outside through the shaft by thermal conduction.

A. Governing Equations

Since the housing and end caps are thermally insulated with rubber gasket that has extremely small thermal conductivity, the rotor and stator can be separately modeled. For the rotor made of solid materials, governing equations in steady-state thermal analysis can be expressed as

$$\frac{\partial}{\partial x} \left(k_x \frac{\partial T}{\partial x} \right) + \frac{\partial}{\partial y} \left(k_y \frac{\partial T}{\partial y} \right) + \frac{\partial}{\partial z} \left(k_z \frac{\partial T}{\partial z} \right) = -q, \quad (4)$$

$$\begin{cases} \Gamma_1 : \frac{\partial T}{\partial x} n_x + \frac{\partial T}{\partial y} n_y + \frac{\partial T}{\partial z} n_z = h(T - T_{amb}) \\ \Gamma_2 : \frac{\partial T}{\partial x} n_x + \frac{\partial T}{\partial y} n_y + \frac{\partial T}{\partial z} n_z = 0 \end{cases} \quad (5)$$

where T is the temperature distribution. k_x , k_y , and k_z are the thermal conductivity along the respective x-, y-, and z-axis directions. For isotropic materials, $k_x = k_y = k_z$. Mechanical and thermal properties of each rotor part sourced from the product manuals are listed in Table V. q is the heat source density, which is directly imported from the above eddy current loss density.

Two kinds of boundary conditions are imposed on rotor surfaces: Γ_1 and Γ_2 , as in (5), where n_x , n_y , and n_z denote the scalar projection of the outward unit normal vector in x-, y-, and z-axis directions. Γ_1 specifies the convection heat transfer coefficient h , between the end caps and ambient air. For conservative consideration, ambient temperature T_{amb} is assumed to be 40 °C, as an additional safety factor for rotor temperature prediction. Heat transfer coefficient of natural convection at the end cap is calculated by (6) [18], where Ra is the dimensionless Rayleigh number for the laminar flow on the surface of vertical flat plate, given by (7).

$$h = 0.59(Ra)^{0.25} k_{air}/d \quad 10^4 < Ra < 10^9 \quad (6)$$

$$Ra = \frac{g\beta}{\alpha\nu} (T_s - T_{amb}) d^3 \quad (7)$$

TABLE VI
THERMAL CONTACT RESISTANCES IN THE NEW ROTOR

Contact resistance	Equivalent air gap (mm)
Rotor hub-shaft	0.015
Endplate-shaft	0.01
Shaft to bearing inner race	0.0087
Bearing outer race to end cap	0.0065

g , α , β , ν , T_s , d , and k_{air} denote the acceleration of gravity, thermal diffusivity of air, thermal expansion coefficient of air, kinematic viscosity of air, average surface temperature of the end cap, characteristic length of the end cap, and thermal conductivity of air respectively. Calculated h is $5.63 \text{ W}/(\text{m}^2 \cdot \text{K})$. Γ_2 is specified for other rotor surfaces that are adiabatic.

B. Determination of Thermal Contact Resistance

Thermal contact resistance between the touching surfaces of two solids usually has a vital influence on heat removal and thus temperature rise [19], [20]. Many researches focused on the unknown resistance by introducing an equivalent average interface air gap δ_{air} [18], [21], [22]. According to these researches, δ_{air} depends on contact pressure, surface roughness, material properties, interface medium, and heat flux density *et al.* Common practice is to select an appropriate value from handbooks or perform an initial calibration test [20]. Equivalent air gaps are determined according to suggestions in these researches, as listed in Table VI (upper limits are used for conservative estimation). These empirical values are valid for the contact of two cylindrical surfaces, and show high accuracy according to experiments in above researches. However, this is not the case for interface between two planes, e.g., the equivalent air gap between the PRS and endplate δ_{air1} , the one between the PM and PRS δ_{air2} , and that between the PM and rotor hub δ_{air3} . These interface air gaps strongly relate to rotation speed and thermal expansion of rotor parts, which make initial calibration tests difficult, if not impossible. Thus, it is hard to determine rational values for δ_{air1} , δ_{air2} , and δ_{air3} . It deserves to be noted that the thermal resistances and thus equivalent air gaps are smaller under rotation condition [23].

For the sake of simplicity, a preliminary parameter sensitivity analysis is carried out to explore the correlation between rotor temperature rise and these contact resistances. To reduce the number of variables and save calculation time, the sum of δ_{air2} and δ_{air3} , denoted by δ_v , is used in the parametric analysis. Conservatively, δ_v is positioned between the rotor hub and PM. Fig. 14 shows the maximum temperatures of the PM and PRS against δ_{air1} and δ_v . Conclusively, rotor temperature rise is insensitive to δ_{air1} , δ_{air2} , and δ_{air3} . The temperature increment is only $7.0 \text{ }^\circ\text{C}$ with the maximal thermal contact resistances. The reason is that rotor eddy current loss in the new rotor is significantly reduced, which causes relatively small temperature drops on these thermal contact resistances.

The bearing is more complicated in terms of heat transfer, due to its complex structure and the presence of grease or oil lubrication. It is hard to develop an exact model for heat transfer through the bearing races. Similarly, an equivalent air gap is

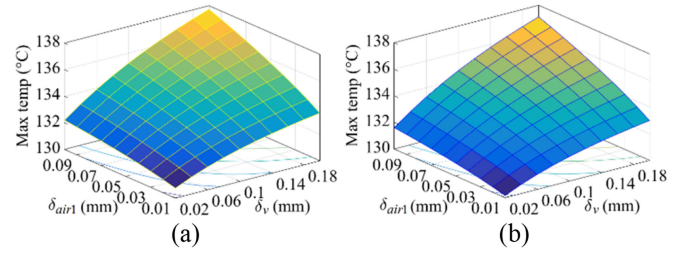


Fig. 14. Maximum temperatures against δ_{air1} and δ_v . (a) Maximum temperature of the PRS. (b) Maximum temperature of the PM.

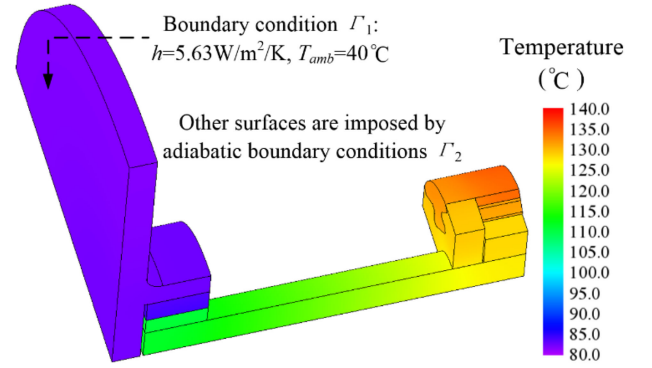


Fig. 15. Temperature distribution and thermal boundaries of the new rotor.

commonly used. Typical values for the equivalent air gap are measured for various bearings in [19], and for bearings in this application, a 0.25 mm interface air gap is used.

C. Predicted Rotor Temperature Distribution

The bearing loss P_{be} is calculated using (8), where n is the rotation speed. T_{be} is the total friction torque obtained from product manual as 0.0029 Nm (using an online calculator offered by bearing manufacturer SKF). Resultant P_{be} for each bearing is 6.85 W , and it is split evenly between the inner and outer races.

$$P_{be} = 2\pi n T_{be} / 60 \quad (8)$$

Temperature distribution and heat flux vector plot when $\delta_{air1} = 0.03 \text{ mm}$ and $\delta_{air2} = \delta_{air3} = 0.05 \text{ mm}$ are shown in Fig. 15 and Fig. 16. The maximum temperature in PM is $131.9 \text{ }^\circ\text{C}$, which is lower than the maximum operating temperature of N35SH. As shown in Fig. 15, temperature drops mainly appear in the long shaft and the bearing. Therefore, downsizing the axial length of FESS and/or using ceramic bearing that has smaller friction loss benefits lowering rotor temperature. Except for the one through PM, the new rotor provides an extra flow path for heat conduction via the endplate to the shaft. Heat fluxes in these two paths are 3.79 W and 4.69 W respectively, i.e., more than half of total heat is dissipated via endplate, as illustrated in Fig. 16.

VI. ROTOR MECHANICAL STRENGTH EVALUATION

Owing to the compact axial size and large shaft diameter, the machine has a 1^{st} critical speed of 37655 r/min with bearing

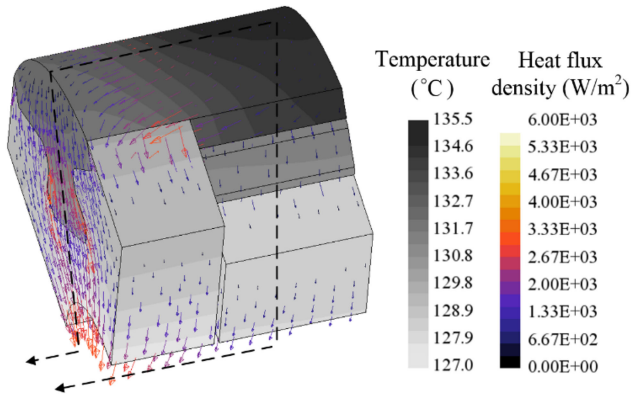


Fig. 16. Temperature distribution and heat flux density of the new rotor from 3-D thermal FEA.

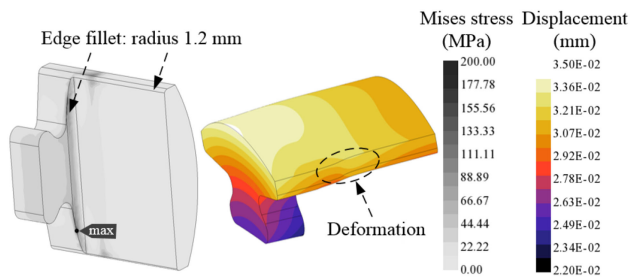


Fig. 17. Von Mises distribution and absolute displacement (scale factor: 250) of the PRS.

support stiffness, according to 3-D modal FEA. The maximum rotation speed is much lower than the critical speed. Therefore, the emphasis of mechanical design is put on evaluating the rotor structure integrity, which is carried out by 3-D structural FEA due to the complex structure of the new rotor. Centrifugal force arising from high-speed rotation and thermal stress resulted from different thermal expansion coefficients and temperature difference in each part are considered. Meanwhile, electromagnetic nodal force imposed on the rotor and the gravity of rotor assemblies are ignored since they are several orders of magnitude less than the above two sources. To take thermal stress into account, rotor temperature distribution from above thermal analysis is directly imported into the structural model in the one-way coupled analysis.

Interference fit is not used in the assembly of rotor components, because the PMs are fixed radially and circumferentially by the PRSs and grooves on the rotor hub, as in Fig. 3. Fillets are created on some edges of the PRS to eliminate potential stress concentration. The Von Mises stress distribution and the displacement of the PRS are shown in Fig. 17. The maximum stress occurs at the fillets and reaches 195.43 MPa at 22500 r/min and steady-state temperature, which is far below the yield strength of Supra 50 of 820 MPa.

Sintered rare-earth magnets are usually considered as brittle materials. They have high compressive strength but low tensile strength. Sintered NdFeB N35SH has a low tensile strength of 82.7 MPa and high compressive strength of 950 MPa. Fig. 18

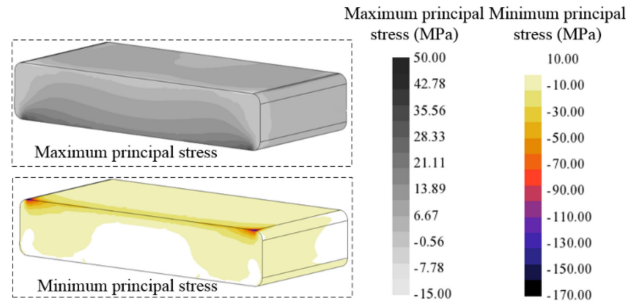


Fig. 18. Maximum and minimum principal stress distributions in PM.



Fig. 19. Manufactured rotor and inductance measurement setups.

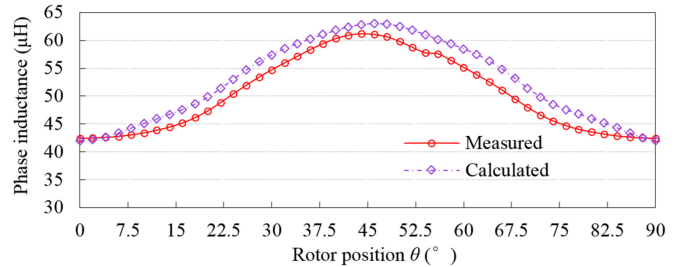


Fig. 20. Calculated and measured phase inductances at different rotor position (θ equals to 0 when rotor d-axis aligns with the axis of measured phase winding).

shows the maximum and minimum principal stress distributions in PM. The maximum principal stress reaches 48.8 MPa, which is under the tensile strength of N35SH with a safety factor 1.5. The difference of thermal expansion coefficient between the rotor hub and PRS, as in Table V, keeps PM compressed at steady-state temperature and high-speed rotation. This can also be observed intuitively in Fig. 17, where obvious deformation in the PRS adjacent to PM appears. In addition, the minimum principal stress is far below the compressive strength of N35SH.

VII. PRELIMINARY EXPERIMENTAL TESTS

A prototype rotor is manufactured to prove the functionality of the new design. To confirm the decrement of magnetic circuit reluctance, phase inductances at different rotor positions are measured with an LCR meter. Measurement setups are shown in Fig. 19. Calculated and measured inductances against rotor position θ are plotted in Fig. 20. The measured inductances achieve satisfactory agreement with the calculated ones, and the small discrepancy may result from an overestimation of the end

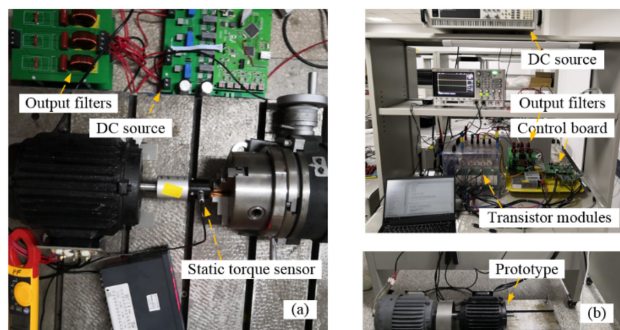


Fig. 21. Experimental setups for (a) static torque measurement and (b) back EMF measurement.

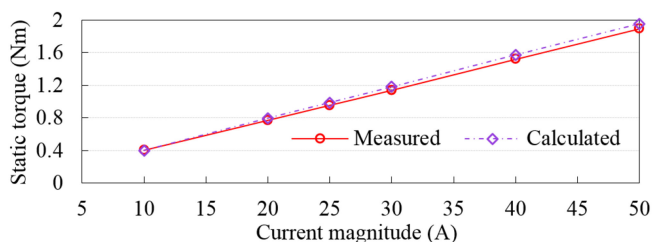


Fig. 22. Measured and Calculated static torques at room temperature (24 °C).

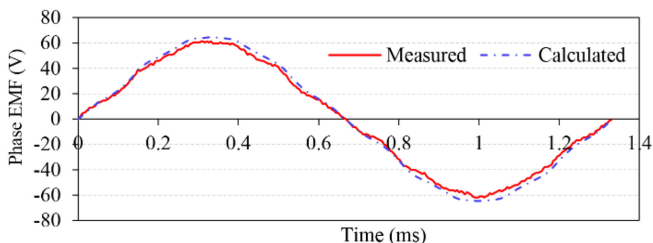


Fig. 23. Calculated and measured back EMFs at 22500 r/min (24 °C).

winding length. It can be seen that the phase inductance varies with θ , i.e., the new rotor shows salient behavior.

Static torques are measured to confirm the torque producing ability of the new rotor. Direct current flows into A-phase winding and out from B- and C-phase windings. Rotor position is determined by a dividing head, and output torque is measured with high-precision torque sensor, as in Fig. 21(a). To eliminate the effect of friction and cogging torques on static torque, two measurements are carried out. One is performed with dc current and another at open circuit. Static torque is obtained by differentiating the results from these two measurements. Measured and calculated torques are compared in Fig. 22. The measured and FEA-predicted results show quite good agreement, and the maximum difference is 3.1%.

Open-circuit back EMF is measured by driving the prototype machine with another HSPMSM in a back-to-back test, as shown in Fig. 21(b). Calculated and measured back EMFs at maximum operating speed are presented in Fig. 23. The amplitude of the measured phase EMF at 22500 r/min is 61.8 V, which agrees well with the FEA-predicted result. In addition, the rotor structure

integrity is well kept at highest operating speed in the back-to-back test.

To measure the rotor eddy current loss and confirm its reduction by experiments, separation of each loss component is essential. However, it is well-known that the separation of rotor eddy current loss from measured total loss is difficult using common loss separation experiments [24], [25]. The reason is that, rotor eddy current loss and stator core loss are concomitant in all measurements. To solve this problem, an indirect method that incorporates a series of measurements are designed. The method measures the heat produced in the rotor to indirectly obtain the rotor loss. Rotor eddy current loss can be obtained by deducting bearing loss from the measured rotor loss. The key to rotor heat measurement is prohibiting heat transfer between the stator and rotor sides, which is available by performing the measurements in a high-vacuum environment.

Similar loss separation method that measures loss by means of vacuum environment has been reported in [26] recently. The vacuum environment and heat measurement require some specialized experimental setups that are being developed. Future works will focus on these tests, and another paper will presents the principle of these measurements, the assembly of experimental setups, and how the measurements are performed.

VIII. CONCLUSION

This paper presents a new rotor design of HSPMSM for flywheel energy storage system. The new rotor aims at reducing rotor eddy current loss that is difficult to be dissipated in a high-vacuum chamber. Electromagnetic performances are analyzed using the finite element method. Besides a 64.2% rotor eddy current loss reduction, the proposed rotor downsizes the effective air gap, which reduces PM usage and increases the inductance of HSPMSM. Rotor temperature analysis results confirm that the loss reduction helps to lower PM temperature rise, and thus low-cost magnets can be used. Taking thermal stress and centrifugal force into account, the strength of the new rotor is confirmed by structural FEA. Prototype measurement results show excellent agreement with FEA-predicted results.

REFERENCES

- [1] B. Dong, K. Wang, B. Han, and S. Zheng, "Thermal analysis and experimental validation of a 30 kW 60000 r/min high-speed permanent magnet motor with magnetic bearings," *IEEE Access*, vol. 7, pp. 92184–92192, Jul. 2019.
- [2] W. Li, Z. Wu, H. Tang, D. Li, and J. Cao, "Research on multi-physical fields of high-power PMSM/G used for FESS during the process of controllable charging and uncontrollable discharging," *IEEE Trans. Energy Convers.*, pp. 1–1, Sep. 2019.
- [3] J. Dong, Y. Huang, L. Jin, and H. Lin, "Comparative study of surface-mounted and interior permanent-magnet motors for high-speed applications," *IEEE Trans. Appl. Supercond.*, vol. 26, no. 4, pp. 1–4, Jun. 2016.
- [4] K. Grace, S. Galioto, K. Bodla, and A. M. El-Refaie, "Design and testing of a carbon-fiber-wrapped synchronous reluctance traction motor," *IEEE Trans. Ind. Appl.*, vol. 54, no. 5, pp. 4207–4217, Sep. 2018.
- [5] T. Wang, Z. Ma, Z. Chen, F. Zhang, and X. Yin, "The research on mechanical properties of direct drive high-speed permanent-magnet machine for compression," in *Proc. 18th Int. Conf. Elect. Machines Syst.*, Oct. 2015, pp. 940–943.

- [6] H. W. Jun, J. Lee, H. W. Lee, and W. H. Kim, "Study on the optimal rotor retaining sleeve structure for the reduction of eddy-current loss in high-speed SPMSM," *IEEE Trans. Magn.*, vol. 51, no. 3, pp. 1–4, Mar. 2015.
- [7] J. X. Shen, H. Hao, M. J. Jin, and C. Yuan, "Reduction of rotor eddy current loss in high speed PM brushless machines by grooving retaining sleeve," *IEEE Trans. Magn.*, vol. 49, no. 7, pp. 3973–3976, Jul. 2013.
- [8] F. Zhang, G. Du, T. Wang, G. Liu, and W. Cao, "Rotor retaining sleeve design for a 1.12-MW high-speed PM machine," *IEEE Trans. Ind. Appl.*, vol. 51, no. 5, pp. 3675–3685, Sep. 2015.
- [9] H. Fang, R. Qu, J. Li, P. Zheng, and X. Fan, "Rotor design for high-speed high-power permanent-magnet synchronous machines," *IEEE Trans. Ind. Appl.*, vol. 53, no. 4, pp. 3411–3419, Jul. 2017.
- [10] S. G. Min and B. Sarlioglu, "Advantages and characteristic analysis of slotless rotary PM machines in comparison with conventional laminated design using statistical technique," *IEEE Trans. Transp. Electrification*, vol. 4, no. 2, pp. 517–524, Jun. 2018.
- [11] Q. Chen, D. Liang, S. Jia, and X. Wan, "Analysis of multi-phase and multi-layer fractional-slot concentrated-winding on PM eddy current loss considering axial segmentation and load operation," *IEEE Trans. Magn.*, vol. 54, no. 11, pp. 1–6, Nov. 2018.
- [12] M. R. Shah and A. M. EL-Refaei, "Eddy-current loss minimization in conducting sleeves of surface PM machine rotors with fractional-slot concentrated armature windings by optimal axial segmentation and copper cladding," *IEEE Trans. Ind. Appl.*, vol. 45, no. 2, pp. 720–728, Mar. 2009.
- [13] J. M. Yon, P. H. Mellor, R. Wrobel, J. D. Booker, and S. G. Burrow, "Analysis of semipermeable containment sleeve technology for high-speed permanent magnet machines," *IEEE Trans. Energy Convers.*, vol. 27, no. 3, pp. 646–653, Sep. 2012.
- [14] W. Li, H. Qiu, X. Zhang, J. Cao, and R. Yi, "Analyses on electromagnetic and temperature fields of superhigh-speed permanent-magnet generator with different sleeve materials," *IEEE Trans. Ind. Electron.*, vol. 61, no. 6, pp. 3056–3063, Jun. 2014.
- [15] H. Fang, D. Li, R. Qu, J. Li, C. Wang, and B. Song, "Rotor design and eddy-current loss suppression for high-speed machines with a solid-PM rotor," *IEEE Trans. Ind. Appl.*, vol. 55, no. 1, pp. 448–457, Jan. 2019.
- [16] J. Zheng, W. Zhao, J. Ji, J. Zhu, C. Gu, and S. Zhu, "Design to reduce rotor losses in fault-tolerant permanent-magnet machines," *IEEE Trans. Ind. Electron.*, vol. 65, no. 11, pp. 8476–8487, Nov. 2018.
- [17] B. Hannon, P. Sergeant, and L. Dupré, "Evaluation of the rotor eddy-current losses in high-speed PMSMs with a shielding cylinder for different stator sources," *IEEE Trans. Magn.*, vol. 55, no. 3, pp. 1–10, Mar. 2019.
- [18] J. P. Holman, *Heat Transfer*, 10 edition. Boston: McGraw-Hill Education, 2009.
- [19] D. Staton, A. Boglietti, and A. Cavagnino, "Solving the more difficult aspects of electric motor thermal analysis in small and medium size industrial induction motors," *IEEE Trans. Energy Convers.*, vol. 20, no. 3, pp. 620–628, Sep. 2005.
- [20] D. P. Kulkarni, G. Rupertus, and E. Chen, "Experimental investigation of contact resistance for water cooled jacket for electric motors and generators," *IEEE Trans. Energy Convers.*, vol. 27, no. 1, pp. 204–210, Mar. 2012.
- [21] R. Camilleri, D. A. Howey, and M. D. McCulloch, "Experimental investigation of the thermal contact resistance in shrink fit assemblies with relevance to electrical machines," in *Proc. 7th IET Int. Conf. Power Electron., Mach. Drives*, Apr. 2014, pp. 1–9.
- [22] A. J. Grobler, S. R. Holm, and G. van Schoor, "Empirical parameter identification for a hybrid thermal model of a high-speed permanent magnet synchronous machine," *IEEE Trans. Ind. Electron.*, vol. 65, no. 2, pp. 1616–1625, Feb. 2018.
- [23] S. Isert, "Heat transfer through a rotating ball bearing at low angular velocities," M.S. thesis, Dept. Mechan. Aeros. Eng., Utah State Univ., Logan, Utah, 2011.
- [24] Z. Huang, J. Fang, X. Liu, and B. Han, "Loss calculation and thermal analysis of rotors supported by active magnetic bearings for high-speed permanent-magnet electrical machines," *IEEE Trans. Ind. Electron.*, vol. 63, no. 4, pp. 2027–2035, Apr. 2016.
- [25] L. Alberti, E. Fornasiero, N. Bianchi, and S. Bolognani, "Rotor losses measurements in an axial flux permanent magnet machine," *IEEE Trans. Energy Convers.*, vol. 26, no. 2, pp. 639–645, Jun. 2011.
- [26] G. Burnand and Y. Perriard, "Very-high-speed miniaturized permanent magnet motors: modeling and validation," in *Proc. IEEE Energy Convers. Congr. Expo.*, 2019, pp. 1–7.



the wheel-hub driving, wind power generation, and servo applications.

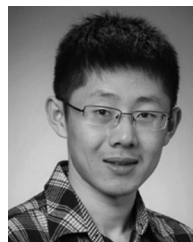


Yunkai Huang received the M.Sc. and Ph.D. degrees in electrical engineering from Southeast University, Nanjing, China, in 2001 and 2007, respectively.

He is currently a Professor with the School of Electrical Engineering, Southeast University. His research interests include design and control of PM machines, particularly the high-speed brushless machine, applications in domestic appliances, electric vehicles, and wind power generation systems are covered.



Jianning Dong (Member, IEEE) received the B.S. and Ph.D. degrees in electrical engineering from Southeast University, Nanjing, China, in 2010 and 2015, respectively. Since 2016, he has been an Assistant Professor with the Delft University of Technology (TU Delft), Delft, The Netherlands. Before joining TU Delft, he was a Postdoctoral Researcher with McMaster Automotive Resource Centre, McMaster University, Hamilton, ON, Canada. His main research interests are design, modeling and control of electromechanical systems.



include optimal design and control of power converters, modeling and digital control of motor drives.



Yu Yao (Student Member, IEEE) received the B.S. degree in electrical engineering from Southeast University, Nanjing, China, in 2016. He is currently working toward the Doctor of Engineering degree in electric machines and control with the School of Electrical Engineering, Southeast University, Nanjing. His main research interests include the design of the power inverter, the current regulator design, the position sensorless drive for the high-speed PMSM, and the drive system with LCL output filter.